

Epitaxial orientation changes in a dewetting gold film on Si(111)R. Daudin,¹ T. Nogaret,² T. U. Schüllli,^{1,3} N. Jakse,² A. Pasturel,² and G. Renaud^{1,*}¹CEA, Institut Nanosciences et Cryogénie, Associated to the Université Joseph Fourier, UJF, SP2M, 17 rue des Martyrs, 38054 Grenoble, France²Laboratoire de Physique et Modélisation des Milieux Condensés, Maison des Magistères, BP 166 CNRS, 38042 Grenoble Cedex 09, France³European Synchrotron Radiation Facility, BP 220, 38043 Grenoble, France

(Received 24 April 2012; revised manuscript received 27 June 2012; published 4 September 2012)

Using *in situ* x-ray diffraction, epitaxial relationships have been measured for different Au deposits on Si(111) surfaces, under ultrahigh vacuum conditions, from room temperature to the eutectic temperature (T_e) of the AuSi binary system. Epitaxies perpendicular to the substrate have been studied for different gold coverages (2, 5, 7, and 20 monolayers). The Au(111) \parallel Si(111) out-of-plane epitaxy was found to be dominant and to present three different in-plane orientation relationships evolving with increasing temperature. These epitaxial variations are induced by the variation of the lattice-parameter misfit with temperature due to differing thermal expansion of the two materials. The temperature dependence of the epitaxial relationship is explained using the coincidence site lattice theory and a study of the “matching quality” at the interface. In addition, *ab initio* calculations have been performed to estimate the stability of the different configurations and compared to the experimental results.

DOI: [10.1103/PhysRevB.86.094103](https://doi.org/10.1103/PhysRevB.86.094103)

PACS number(s): 68.55.A–, 61.05.C–

I. INTRODUCTION

Thin films and nanostructures of noble metals on semiconductor substrates are the subject of numerous studies^{1,2} because of their importance in semiconductor technology. Among these there is the peculiar AuSi system, which presents a deep eutectic point ($T_e = 636$ K, $x_{\text{Si}} = 18.6$ at.%), and in which the metal used as a catalyst offers a convenient way to grow semiconductor nanowires on silicon through the well-known VLS (vapor-liquid-solid) process.^{3,4} Nanowires are of great interest because of their new properties and potential applications arising from their reduced lateral size. Their physical properties are intimately linked to their structural characteristics such as shape, size, atomic structure, composition, or defects, which depend on the preparation conditions (deposition method, flux, temperature, nominal or structured substrates). In particular, their size is strongly linked to that of the solid Au nanocrystals which catalyze their growth on the Si substrate.⁵ Moreover, an unusually large supercooling of AuSi eutectic droplets on Si(111) was recently reported⁶ under certain conditions, in which the Si(111) surfaces undergo a Au-induced (6×6) reconstruction. This preservation of the melted state of Au islands well below the eutectic temperature could help grow nanowires at lower temperatures. Interestingly, also, the existence of crystalline surface phases of the liquid AuSi eutectic alloy has been reported recently.^{7–9} These observations call for a better understanding of the structure of gold films and islands on Si(111) and of their interface with Si(111).

Many characterization methods have been used to shed light on various aspects of this system: from the structure determination and conditions of formation of surface reconstructions^{10–12} to the understanding of the growth mode,^{13–15} the wetting/dewetting behavior,^{16,17} islands/droplets formation (size, dispersion, shape),^{18,19} surface gold atoms diffusion,²⁰ or the structure of the interface.^{21,22} Attention is now focused on the understanding of the microscopic

phenomena that take place in the gold droplet on top of a silicon nanowire during their VLS growth.²³

Only few studies concentrate on the epitaxial relationships. Vasisht *et al.*²⁴ reported only the “cube on cube” epitaxy for a 75-nm-thick gold film on Si(111). Warren *et al.*²⁵ studied the growth mode of gold on Si(111)-H surfaces for different gold thicknesses [1.75 to 18.6 monolayers (ML)] and evoked rotated or unrotated island with respect to the substrate’s directions. To the best of our knowledge, only Chen *et al.*²⁶ observed three “modes” of Au epitaxy on Si(111), but for a 40-nm film and only around 600 K, with no temperature dependence reported.

In this paper, grazing incidence x-ray scattering²⁷ (GIXS) is used *in situ*, in UHV (ultrahigh vacuum), to characterize the epitaxial relationships of a gold film deposited at room temperature (RT) on a Si(111) substrate, and their evolution upon heating until melting at T_e . It reveals the dominance of the Au(111) \parallel Si(111) out-of-plane configuration for the different gold coverages (2, 5, 7, and 20 ML). Moreover, this predominant out-of-plane epitaxy presents three different in-plane orientation relationships (ORs) labeled OR1, OR2, and OR3, the occurrence of which depends on temperature. The selection of the preferred OR is found to depend on the matching quality of the coincident sites at the gold/silicon interface, as confirmed by *ab initio* simulations.

II. EXPERIMENTAL AND SIMULATION METHODS**A. Experimental methods**

The sample preparation and the x-ray experiments were carried out at the ESRF (European Synchrotron Radiation Facility, Grenoble, France) on the BM32 beamline, using a chamber devoted to surfaces, interfaces, and nanostructures studies under ultrahigh vacuum coupled to a surface diffractometer. Before each experiment, the 10×10 mm² Si(111) samples were placed in a preparation chamber and outgassed at 500 K during 24 h to remove organic impurities before being transferred into the growth chamber under UHV. This

UHV chamber, base pressure 10^{-10} mbar, is equipped with large beryllium windows which give the possibility to the x-ray beam to reach the sample and to measure the scattered radiation over a large solid angle.

The temperature of the sample is controlled by electron bombardment under the sample holder and measured with two IRCON infrared pyrometers, placed outside the chamber behind a sapphire viewport, covering together a temperature range from 470 to 2200 K. They were previously calibrated in the temperature regime covered by this study at the melting points of ultrapure lead (600 K) and of bulk $\text{Al}_{88}\text{Si}_{12}$ eutectic (850 K). Moreover, whatever the amount of Au deposited and the sample history, the Au islands were always found to melt at the AuSi eutectic temperature of 636 K. The accuracy of the temperature measurement is evaluated to ± 5 K. Note that no change of the measured temperature was found during dewetting of the Au film, which indicates that the thin Au films do not significantly change the sample emissivity.

The Si samples were deoxidized at 1200 K under UHV conditions (10^{-10} mbar), and then characterized *in situ* by reflection high-energy electron diffraction (RHEED) and GIXS. Both revealed a clear diffraction pattern corresponding to the formation of a well-defined $\text{Si}(111)-(7 \times 7)$ surface reconstruction, which is the typical sign for a clean $\text{Si}(111)$ surface.²⁸ The typical size of the reconstruction domains, as determined by the width of the reconstruction peaks, was of the order of $1 \mu\text{m}$. 2, 5, 7, or 20 ML of gold were evaporated on the sample at RT using a Knudsen cell with a flux of 0.4 \AA min^{-1} . In this study, one monolayer (ML) of gold corresponds to a deposited thickness of (2.35 \AA), i.e., the distance between two $\text{Au}(111)$ planes in bulk Au, assuming the gold monolayer density is identical to that of the $\text{Au}(111)$ planes. The deposition rate was calibrated using a quartz microbalance and x-ray reflectivity. The $\text{Si}(111)-(7 \times 7)$ reconstruction is found to disappear for deposited thicknesses larger than 2 ML, indicating a strong metal/substrate interaction.

GIXS (Ref. 27) was performed with an 11-keV incident beam at a fixed incident angle α_i of 0.163° , equal to the critical angle for total external reflection for silicon at this energy, to enhance surface versus bulk scattering. The intensity was measured up to a maximum value of 8.5 \AA^{-1} of the momentum transfer. This latter is defined as $\mathbf{Q} = \mathbf{k}_f - \mathbf{k}_i$, \mathbf{k}_i and \mathbf{k}_f being the wave vectors of incident and scattered beams, respectively, so that $\|\mathbf{Q}_\parallel\| = (4\pi/\lambda) \sin(\delta/2)$, where δ is the scattering angle between the projections of \mathbf{k}_i and \mathbf{k}_f on the reference surface, and λ the x-ray wavelength. In this paper, we call *rocking scan* a scan performed by a rotation ω of the sample around its surface normal at a constant Q (i.e., with all other angles fixed). A *radial scan* is a scan performed along a given substrate direction with fixed α_i and α_f . Out-of-plane scans along $Q_\perp = k[\sin(\alpha_i) + \sin(\alpha_f)]$ (defined here without taking refraction into account) are performed by varying α_f with fixed α_i and called *Q_\perp scans*. Each scan gives structural information in the direction of the measurement.

B. Simulations

To model energetic effects related to the in-plane epitaxial relationships of gold film on a $\text{Si}(111)$ substrate, we performed total-energy calculations using the density-functional theory

(DFT) as implemented in the Vienna *ab initio* simulation package.²⁹ Projected augmented plane wave³⁰ (PAWs) with the Perdew-Wang exchange-correlation potential were adopted. The valence state of each element has been defined previously in the provided PAW potentials and the plane-wave cutoff was 300 eV. Numerical integrations in the Brillouin zone were performed by means of the Hermite-Gaussian method with $N = 1$ and smearing parameter of $\sigma = 0.1$ eV.

We used three different supercells representative of the experimentally measured in-plane orientations, i.e., OR1, OR2, and OR3. They are constituted of a 10-\AA vacuum layer and four Au layers on top of six $\text{Si}(111)$ bilayers. The dangling bonds of Si atoms of the bottom are hydrogenated. The supercells contain 181, 80, and 139 atoms for OR1, OR2, and OR3 configurations, respectively. Brillouin-zone sampling using a $4 \times 4 \times 2$, $6 \times 6 \times 3$, $5 \times 5 \times 2$ k -point grid was found necessary for differences of total energies of the OR1, OR2, OR3 supercells, respectively, to converge within 10^{-3} eV. Structural optimizations were carried out under the conditions that all residual forces should be smaller than 0.01 eV/\AA .

III. RESULTS

Figure 1(a) shows a long *radial scan* along the $\text{Si}[1\bar{1}0]$ direction performed at RT after a deposit of 7 ML. It displays two Bragg peaks of the silicon single-crystal substrate and several Bragg peaks from gold, indicating that the deposited thin film is a polycrystal. The gold peaks can be gathered into three families corresponding to three types of interface orientation perpendicular to the surface: $\text{Au}(111) \parallel \text{Si}(111)$ (type A in red), $\text{Au}(1\bar{1}0) \parallel \text{Si}(111)$ (type B in green), and $\text{Au}(00\bar{1}) \parallel \text{Si}(111)$ (type C in blue). Some peaks belong to more than one type. For instance, the Au peak at 4.36 \AA is representative of the $\{220\}$ plane family, but we will see later that perpendicular measurements allow us to define the complete epitaxial relationship and thus label it more precisely. Hence, $\text{Au}(2\bar{2}0)$, $\text{Au}(111)$, and $\text{Au}(200)$ peaks are taken as signatures of types A, B, and C, respectively. For convenience, we will use these three peaks in the following discussion.

Figure 1(b) shows *radial scans* along the $\text{Si}[1\bar{1}0]$ direction performed at RT for different deposited amounts. For 2 ML, no clear crystalline gold peak is recorded so that no out-of-plane epitaxial mode can be deduced at RT. The special case of low deposits (up to 2 ML) is discussed in a separate part in Sec. IV. For 5 ML, only the $\text{Au}(2\bar{2}0)$ peak is present, which means that only the A-type epitaxy takes place. For 7 ML, the $\text{Au}(111)$ and the $\text{Au}(200)$ peaks appear (i.e., B and C types appear), but the $\text{Au}(2\bar{2}0)$ peak is still the most intense (i.e., epitaxy A is predominant). For higher coverage (20 ML), the three modes coexist with still a majority of the gold structures in A-type epitaxy [the $\text{Au}(111)$ planes parallel to the $\text{Si}(111)$ substrate]. This shows that the out-of-plane epitaxy type depends on the coverage. During the RT growth, the first few Au monolayers adopt the A-type epitaxy. Other minority epitaxies appear only for deposits larger than 5 ML. The A-type epitaxy is always dominant, the $\text{Au}(2\bar{2}0)$ peak being the most intense. Let us now concentrate on the evolution of these epitaxies upon annealing.

The *radial scans* performed along the $\text{Si}[1\bar{1}0]$ direction presented in Fig. 2(a) were recorded at RT and 600 K for a deposit of 5 ML. As already mentioned, at RT, only the A-type epitaxy

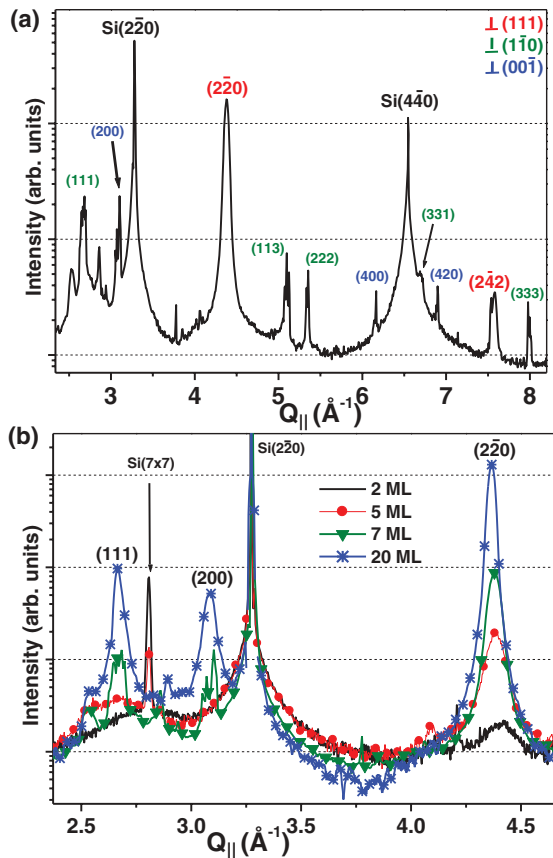


FIG. 1. (Color online) (a) *Radial scan* along the Si[110] direction after a 7-ML deposit of gold at RT. Both scans display the logarithm of the intensity as a function of momentum transfer amplitude. The red, green, and blue colors emphasize the three types of interface orientation perpendicular to the surface deduced from each peak. They are, respectively, Au(111) || Si(111) (type A), Au(110) || Si(111) (type B), and Au(001) || Si(111) (type C). (b) *Radial scan* along the Si[110] direction at RT for deposits of 2 ML (black), 5 ML (red/disks), 7 ML (green/triangles), and 20 ML (blue/stars).

is observed. The corresponding *radial scans* at 600 K (36 K below the AuSi eutectic temperature) show that the intensity of Au(111) and the Au(220) peaks increases and that the Au(200) peak appears. Hence, annealing at higher temperature induces a better crystalline quality and a modification of the epitaxial relationships as discussed in details below.

Figure 2(b) shows *radial scans* recorded at 620 K along two directions Si[110] and Si[121] for a 5-ML deposit. It reveals that the film displays different in-plane orientations as the intensity of the different peaks changes between the two directions. When the temperature is further increased at 640 K, i.e., above T_e , the Si atoms diffuse into the gold islands to reach the eutectic composition (Au₈₁Si₁₉). No more gold Bragg peaks are seen and a liquid signal is recorded: the islands turn into liquid droplets.

The in-plane orientations are more accurately revealed on a reciprocal space map (Fig. 3) measured at 620 K, just before melting, by recording the intensity in a sector located between the Si[110] and Si[121] axes. The Si(220) Bragg peak is clearly visible, together with Debye-Scherrer rings of

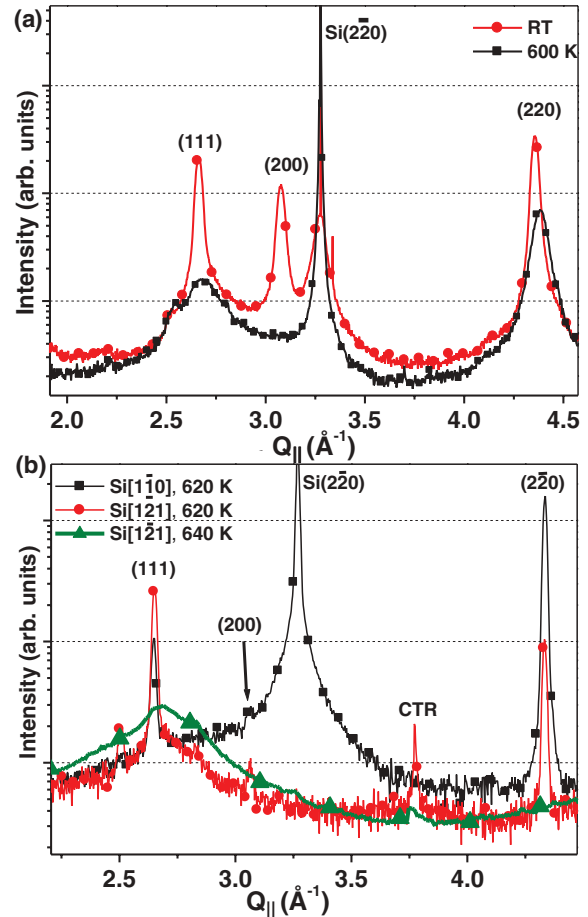


FIG. 2. (Color online) (a) *Radial scan* along the Si[110] direction after the deposit of 5 ML of gold at RT (black/squares) and after annealing at 600 K (red/disks). (b) *Radial scan* along the Si[110] (black/squares) and the Si[121] directions at 620 K (red/disks) and 640 K (green/triangles) after a deposit of 5 ML at RT. Logarithm of intensity as a function of the in-plane momentum transfer.

polycrystalline gold [Au(111), Au(200), and Au(220)]. The intensity of the Au(220) ring presents maxima for different in-plane directions, revealing a texture with additional favorable

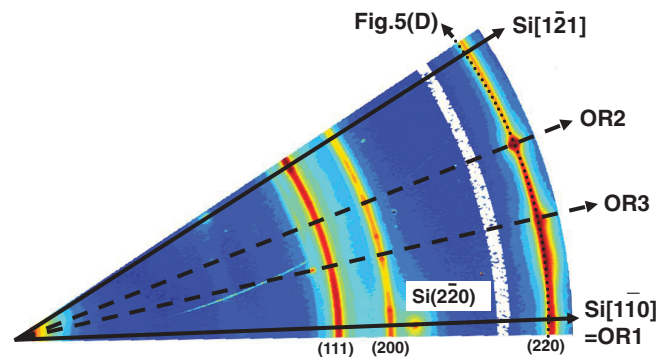


FIG. 3. (Color online) In-plane reciprocal space map covering 30° of the reciprocal space (red: high intensity; blue: low intensity; yellow: intermediate) recorded at 620 K for a sample onto which 5 ML were deposited at RT. The white ring corresponds to a loss of the synchrotron beam during the acquisition time.

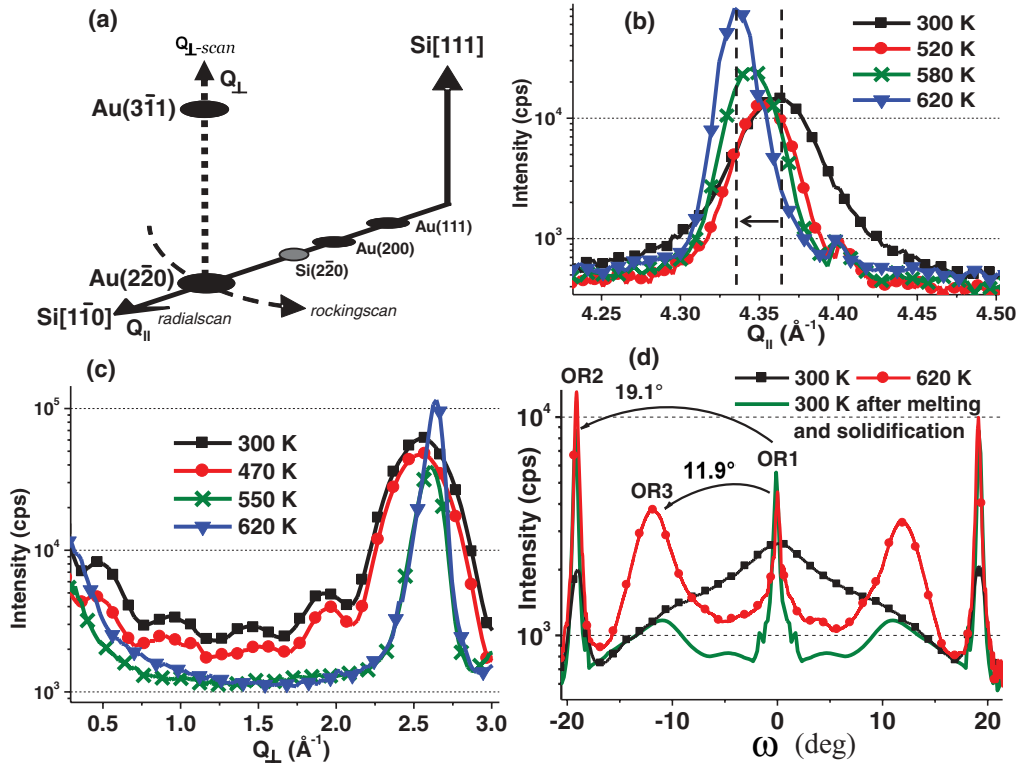


FIG. 4. (Color online) (a) Scheme of the measurements performed in reciprocal space around the Au(220) peak. (b) *Radial scans* on the Au(220) peak along the Si[110] direction at 300 K (black/squares), 520 K (red/disks), 580 K (green/crosses), and 620 K (blue/triangles); the shift of the peak shows the expansion of gold with annealing. (c) Q_{\perp} scans crossing the Au(311) Bragg peak for equivalent temperatures as in (b), illustrating the dewetting of the gold film during heating. (d) *Rocking scans* on the Au(220) ring at 300 K (black/squares), 620 K (red/disks), and again at 300 K after melting and subsequent cooling (green/no symbols). The peaks correspond to the directional relationships in the plane between the gold and the silicon substrates. All measurements were performed in the case of a 7-ML deposit.

in-plane orientations with respect to the ones observed by comparing the scans along the two directions in Fig. 2(b). This indicates that for the dominant A-type epitaxy [Au(111) \parallel Si(111)], different in-plane orientation relationships can be found. We thus focus on the A-type out-of-plane epitaxy, which reveals a systematic behavior of the evolution of its in-plane ORs with temperature.

Figure 4(a) is an illustration of different scans performed around the Au(220) peak to characterize the 7-ML gold film structure and its behavior with temperature ranging from 300 to 620 K (16 K below T_e). *Radial scans* on the Au(220) peak [along the Si[110] direction, Fig. 4(b)] and Q_{\perp} scans on the Au(311) [Fig. 4(c)] are, respectively, sensitive to the average in-plane and out-of-plane lattice parameters; *rocking scans* on the Au(220) Debye-Scherrer ring [Fig. 4(d)] probe different in-plane rotational variants of A-type epitaxy.

Figure 4(b) shows the radial evolution of the Au(220) peak with temperature. At 300 K, the peak is located at $Q_{\parallel} = 4.36 \text{ \AA}^{-1}$, which is the exact location expected at RT, given by $Q = (2\pi\sqrt{h^2 + k^2 + l^2})/a_{\text{Au}}^2$, with $a_{\text{Au}} = 4.079 \text{ \AA}$ the lattice parameter of gold at 300 K and (h,k,l) the Miller's indexes. The corresponding Au crystals are thus not strained. Upon heating, the peak shifts from 4.36 to 4.33 \AA^{-1} at 620 K, illustrating the expansion of gold with increasing temperature. From measurements of different Au peaks, an average value of $\alpha_{\text{Au}} = 15 \times 10^{-6} \text{ K}^{-1}$ is deduced for

the linear thermal expansion coefficient of gold, in good agreement with literature.³¹ One can also notice an increase of the peak height and a narrowing of the full width at half maximum (FWHM), revealing the growth of these crystallites thanks to higher atomic mobility as the temperature increases.

Q_{\perp} scans at the Q_{\parallel} value of the Au(220) peak are reported in Fig. 4(c). A peak around $Q_{\perp} = 2.5 \text{ \AA}^{-1}$ is found, corresponding to the Au(311) Bragg position, which confirms that the Au(111) planes are parallel to the Si(111) planes. At 300 K, the peak width (FWHM = 0.37 \AA^{-1}) and the oscillation period confirm a film thickness of 16.8 \AA (~ 7 ML) with a low roughness. With increasing temperatures, the oscillations disappear and the Au(311) peak becomes narrower, which, together with grazing incidence small-angle x-ray scattering (GISAXS) measurements reported elsewhere³² reveal that the film first gets rougher before the dewetting process takes place: the film turns into islands. At 620 K, the FWHM of the peak is 0.09 \AA^{-1} , which corresponds to an average island's height of about 70 \AA . Along Q_{\perp} , the Au(311) Bragg peak is found at the expected position for Au at 620 K, while at 300 and 470 K, the peak is much closer to the origin. This is tentatively explained by a larger interlayer spacing in the few-ML-thick film, especially in the outer layers, due to surface and/or interface relaxation. The *rocking scans* on the Au(220) Debye-Scherrer ring provide information on the

in-plane crystallographic orientations of the grains composing the gold film and/or the gold islands. As shown in Fig. 4(d), at 300 K the scan displays a large and broad peak centered on the Si[1 $\bar{1}$ 0] direction and two narrow satellite peaks (which are equivalent by symmetry) at $\pm 19.1^\circ$ corresponding to the Si[2 $\bar{3}$ 1] in-plane direction. This reveals two preferred in-plane orientations of the gold structures with respect to the substrate at 300 K. The first orientation relationship (OR1), related to the central peak, is [1 $\bar{1}$ 0]Au(111) \parallel [1 $\bar{1}$ 0]Si(111) and corresponds to identical orientation of the Au crystals and the Si substrate. The second orientation relationship (OR2), rotated in the plane by 19.1° , is [2 $\bar{3}$ 1]Au(111) \parallel [1 $\bar{1}$ 0]Si(111), for which the [2 $\bar{3}$ 1] rows of Au are parallel to the Si[1 $\bar{1}$ 0] axis. At 300 K, a majority of the grains ($\sim 92\%$) are in the OR1 configuration as deduced from the integrated intensity.

After annealing the sample at 620 K and dewetting of the film into islands (still solid), a new peak arises at $\pm 11.9^\circ$ [Fig. 4(d)], attesting to the emergence of a third epitaxial orientation (called OR3) of gold islands with the silicon substrate. This epitaxial orientation could be either the [7 $\bar{9}$ 2]Au(111) \parallel [1 $\bar{1}$ 0]Si(111) relationship already reported by Chen *et al.*,²⁶ which would yield a peak at 12.21° , or the [4 $\bar{5}$ 1]Au(111) \parallel [1 $\bar{1}$ 0]Si(111), which would yield a peak at 10.89° . We will see later that the latter is the correct one, and that it should be rewritten as [1 $\bar{2}$ 1]Au(111) \parallel [2 $\bar{3}$ 1]Si(111). We can also notice that at 620 K, the central peak is narrower and less intense than the 19.1° one. From the integrated peak intensity, we deduce that half of the islands now adopt the OR2 configuration. Hence, the dewetting process taking place from RT to 620 K is accompanied by a change in the epitaxial relationships from OR1 to OR2 and by the appearance of the OR3. For an initial 7-ML-thick deposit at RT, the crystalline domains of OR2 orientation at 620 K have an average in-plane size of 300 Å, as estimated from the rocking scans width of two diffraction peaks at different Q values, and a thickness of 70 Å, as estimated from the FWHM of a Q_\perp scan on a corresponding out-of plane (3 $\bar{1}$ 1) peak.

IV. DISCUSSION

A. Growth mode at RT and dewetting process

The Q_\perp scans plotted in Fig. 4(c) show that the 7-ML deposit of gold at RT consists of a flat film. The growth of Au on Si(111) substrates was reported to follow a Stranski-Krastanow (SK) mode [wetting layer + three-dimensional (3D) growth] at relatively high temperature (above 500 K),^{13,15,33,34} but also sometimes at RT.¹⁸ A quasi-Frank-van der Merwe (FM) growth mode (layer-by-layer growth on several disordered layers) has also been reported for deposits performed at a low temperature of 100 K,³⁵ and 3D or 2D growth has been observed at RT depending on the substrate quality.³⁶ Au is also known to grow layer by layer at RT on the low-density plane Si(001).³⁷ In the experimental conditions of this study, the observation of an epitaxial film of 7 ML claims for a FM growth mode at RT.

The interface energy between the substrate and the growing film depends on the interaction energy between the two crystals. Following Lojkowski *et al.*,³⁸ the interface energy

(γ_I) between gold and silicon is given by

$$\gamma_I = \gamma_{\text{Si}} + \gamma_{\text{Au}} - \gamma_{\text{adh}}, \quad (1)$$

where γ_{adh} is the adhesion energy. Therefore, the most stable interface (small γ_I) corresponds to small γ_{Si} and γ_{Au} values and large γ_{adh} ones. For Si, the (111) plane has the lowest surface energy as it is the densest. For face-centered-cubic metals such as gold, the low-energy surfaces are closely packed planes, with $\gamma_{\text{Au}(111)} < \gamma_{\text{Au}(001)} < \gamma_{\text{Au}(011)}$ (Ref. 39), which explains why the Au(111) \parallel Si(111) epitaxy (type A) is energetically favored and thus the prominent epitaxy. In a following part (see Sec. IV B), we will show that γ_{adh} is the driving force to explain the stability of the different ORs.

When annealing at increasing temperatures (below T_e), the flat film turns into islands [Fig. 4(c)]. The dewetting process, which is assumed to start at the grain boundaries of the films,¹⁶ is driven by the minimization of the surface-to-volume ratio and is a diffusion-limited process. As a consequence, the atomic mobility offered by the annealing allows the system to reduce its surface area through agglomeration of the atoms.¹⁶ The increase of the gold Bragg peaks intensity [Fig. 2(a)] with increasing temperature reveals the changes that take place in chemical bondings to form Au-Au instead of Au-Si bonds. Generally, the dewetting process, which occurs in the solid state, leads to crystalline islands distributed on a wetting layer,²³ although there are some exceptions without wetting layers.⁴⁰

1. Case of 2-ML deposits

Let us study here the peculiar case of a small deposit. For the 2-ML deposit at RT, Fig. 1(b) displays gold peaks that are broad and present low intensity reminding of an amorphous signature. They can also indicate the presence of very small crystal grains. These measurements indicate a gold film of poor crystalline quality into which Au-Si bonds may be preferred to Au-Au bonds, thus lowering γ_I . This observation agrees well with the process proposed by Yeh *et al.* as well as Hoshino *et al.* who measured that for small Au deposits (below 2~3 ML), an Au-Si alloy film forms at RT.^{41,42} For subsequent deposition, their studies pointed out that the nucleation of the gold film occurs below the alloy with an abrupt Au/Si(111) interface. The appearance of the Au(2 $\bar{2}$ 0) peak for 5 ML [Fig. 1(b)] supports this idea.

Note here that for a 2-ML deposit, OR1 was found to be the preferred in-plane orientation after annealing at 620 K. As a lower deposit leads to smaller islands, a possible link between island size and in-plane orientation can not be excluded.³² The widths of *rocking scans* on the in-plane Au(2 $\bar{2}$ 0) and Au(2 $\bar{4}$ 2) Bragg peaks are dominated by the domain-size contribution, yielding an in-plane size of 150 Å, and the Q_\perp scans on the Au(3 $\bar{1}$ 1) peak yield a 40-Å height. Both values are consistent with the island size and height deduced from grazing incidence small-angle x-ray scattering measurements reported elsewhere.³²

B. In-plane orientation relationships (for deposits larger than 2 ML)

As the interface between Au and Si(111) is known to be sharp (i.e., without intermixing)⁴¹ below the eutectic

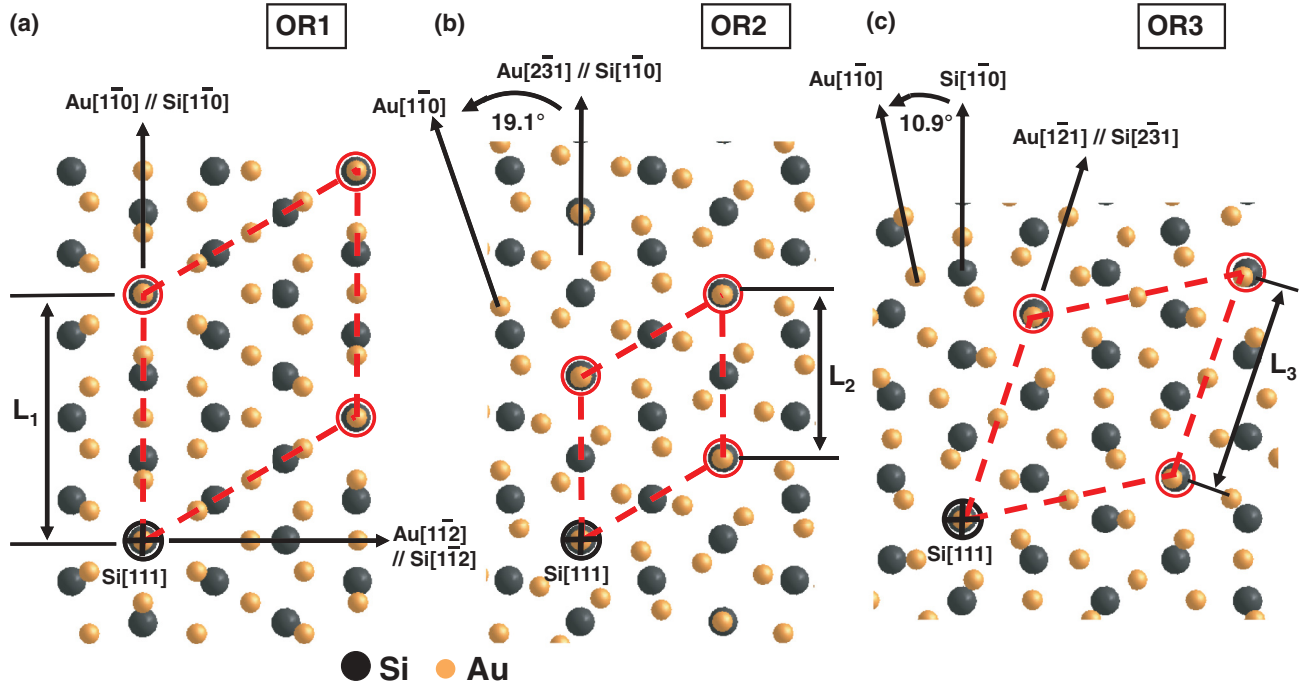


FIG. 5. (Color online) Plane view of the interface represented by the superposition of the Au(111) plane (yellow/bright atoms) above the Si(111) plane (black/dark atoms), the lattice-parameter values are taken at 300 K. The Au(111) plane is rotated around the Si[111] axis by 0° (OR1) (a), 19.1° (OR2) (b), and 10.9° (OR3) (c). The atoms marked with a black cross are in coincidence. For each case, the coincidence site lattice is plotted in red (dashed) and the periodicity (L_x) is indicated. It reveals that $L_2 < L_3 < L_1$.

temperature, let us focus on the way the Au(111) plane is related to the substrate for the three epitaxial ORs in terms of atomic matching in real space. The lattice parameters of the two crystals ($a_{\text{Si}} = 5.431 \text{ \AA}$ and $a_{\text{Au}} = 4.079 \text{ \AA}$, at 300 K) differ largely, resulting in a large misfit $\psi = 2|a_{\text{Au}} - a_{\text{Si}}|/(a_{\text{Au}} + a_{\text{Si}}) = 0.28$, and hence in a poor atomic matching. The three epitaxial configurations revealed by x-ray are represented in real space in Fig. 5 by superposing the Au(111) plane (yellow/bright atoms) with the Si(111) plane (black/dark atoms) at 300 K.

Figure 5(a) corresponds to the OR1 configuration in which the $[1\bar{1}0]$ rows of the two crystals are parallel. In this configuration, each fourth atom of the Au $[1\bar{1}0]$ row coincides with the third atom of the Si $[1\bar{1}0]$ one. The rotations by 19.1° and 10.9° of the Au(111) planes around the $[111]$ axis bringing the system into OR2 and OR3 configurations are represented in Figs. 5(b) and 5(c), respectively. For OR2, the first atom of the Au $[2\bar{3}1]$ row is in good coincidence with the second of the Si $[1\bar{1}0]$ row. For OR3, the coincidence is almost achieved for the second atom of the Au $[1\bar{2}1]$ row with the first of the Si $[2\bar{3}1]$ row. Note that the third epitaxy is identical to that already reported by Chen *et al.*, written as $[7\bar{9}2]\text{Au}(111) \parallel [1\bar{1}0]\text{Si}(111)$. Our notation $[1\bar{2}1]\text{Au}(111) \parallel [2\bar{3}1]\text{Si}(111)$ emphasizes the parallel rows of the two crystals along which the coincidence sites are found.

A common geometrical criterion to study epitaxial relationships, proposed by Bollmann *et al.*⁴³ and developed in subsequent studies,^{44,45} is called “coincidence site lattice” (CSL). It consists in bringing the two different lattices into partial self-coincidence such as done in Fig. 5. The common

lattice sites form the nodes (the “O points”) of a superlattice. The OR1 case reveals a hexagonal CSL (highlighted in red/dashed) of periodicity L_1 (11.52 \AA). The OR2 and OR3 configurations lead to CSLs of periodicities L_2 (7.68 \AA) and L_3 (10 \AA), respectively.

According to Lojkowski *et al.*,³⁸ the adhesion energy is linearly linked with the bonding energy E_{AuSi} between Si and Au atoms “in position of good matching” as follows³⁸:

$$\gamma_{adh} = \eta \frac{E_{\text{AuSi}}}{\Omega^{2/3}}, \quad (2)$$

where Ω is the average atomic volume and η represents the fraction of perfect bonds³⁸ and can thus be seen as the degree of good matching between the two planes. Equation (2) means that the better the matching, the higher γ_{adh} , the lower the interface energy [Eq. (1)]. The preferred orientation relationship (OR) corresponds to the maximum density of approximate CSL nodes (O-lattice nodes), i.e., to a large η in Eq. (2) and therefore to a low interface energy.

According to the O-lattice criterion of Bollmann and the related interface energy, the OR2 should thus be favored with respect to the OR3, itself more favorable than the OR1 as $L_2 < L_3 < L_1$. If OR2 is indeed the preferred orientation relationship at 620 K, this is not the case at RT, where the OR1 is more favorable. To understand this effect, one must take a closer look to what extent the “good matching” really is and how it evolves with temperature: the O-lattice theory has to be refined by taking the OR mismatch into account. The OR mismatch represents the relative difference between the theoretical perfect coincidence point and the real places where

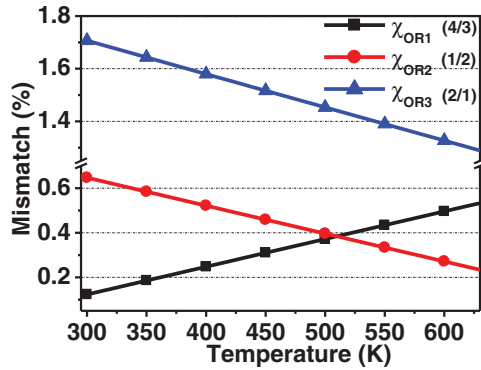


FIG. 6. (Color online) Temperature dependence of the mismatch value χ for the three ORs: χ_{OR1} (black/squares), χ_{OR2} (red/circles), χ_{OR3} (blue/triangles). The ratio m/n is given in the caption next to the concerned epitaxy.

the gold atoms are located. It can be expressed as

$$\chi_{ORx} = \frac{|i \times d_{Au[hkl]} - j \times d_{Si[h'k'l']}|}{(j \times d_{Si[h'k'l']})}, x \in (1,2,3) \quad (3)$$

where $d_{Au[hkl]}$ and $d_{Si[h'k'l']}$ are the distances between two atoms in the gold $[hkl]$ and silicon $[h'k'l']$ rows, respectively (for example, $d_{Si[1\bar{1}0]} = 3.84 \text{ \AA}$ at 300 K). i is the i th atom of the considered gold row that matches the j th atom of the Si row.

In this range of temperature, the thermal expansion coefficients of the two materials can be considered as constant but have very different values: $\alpha_{Au} = 14.5 \times 10^{-6} \text{ K}^{-1}$ and $\alpha_{Si} = 2.6 \times 10^{-6} \text{ K}^{-1}$. As a consequence, gold expands much more than silicon and the mismatch values are modified upon heating (Fig. 6). At 300 K, $\chi_{OR1} = 0.12\%$ and $\chi_{OR2} = 0.65\%$, the shortest periodicity is thus offered by the OR2 relationship, but the best matching is achieved by the OR1 one. As far as the OR3 is concerned, its mismatch value is so high ($\chi_{OR3} = 1.7\%$) that no grain presents this epitaxial orientation. With increasing temperature, χ_{OR2} decreases (as well as χ_{OR3}) and χ_{OR1} increases, a crossover being found around 500 K. At 620 K, $\chi_{OR1} = 0.52\%$ and $\chi_{OR2} = 0.25\%$, therefore, the OR2 configuration is preferred with respect to the OR1, and the OR3 emerges because its mismatch value is reduced. Here, the experimental measurements clearly underline that the prevailing criterion for the Au/Si(111) interface in this experiment is the “matching quality.”

To confirm this experimental view, we performed *ab initio* calculations at $T = 0 \text{ K}$ to determine the energetic properties of the three ORs. Their calculated formation energies referred to bulk Au and Si as well as their interface energies are gathered in Table I. OR2 presents the lowest formation energy as well as the lowest interface energy, and should thus be favored. However, this conclusion has to be moderated because pure Au and Si lattice parameters provided by DFT, of 4.137 and 5.463 \AA , respectively, exceed the experimental ones at 0 K by 1.4% and 0.6%, respectively, leading to OR mismatches of 1.1%, 0.34%, and 0.8% for OR1, OR2, and OR3, respectively. The lower energies for OR2 are likely induced by the lower mismatch, i.e., the “better match” between Si and Au atomic positions. Indeed, the calculated lattice parameters,

TABLE I. Formation and interface energies obtained by *ab initio* calculations for the different ORs. The lowest energies, indicated in bold, correspond to OR2.

OR	Formation energy (J m^{-2})	Interface energy (J m^{-2})
OR1	0.886	0.221
OR2	0.857	0.192
OR3	0.908	0.243

and hence mismatch, would correspond to the experimental high-temperature situation, for which the hierarchy (OR2 more stable than OR1 more stable OR3) is found. Because the calculated interface energies of OR1 and OR2 are very similar, it is likely that the interface energy of OR1 would become smaller at low temperature if we would correct for the inexact lattice parameters and thus OR mismatch values.

Hence, the DFT calculation is in good qualitative agreement, both for the energies and the OR mismatch, with the experimental results at 620 K. A correction of the calculated lattice parameters would also provide a good agreement at 300 K. These conclusions confirm the above proposed arguments based on lower coincidence site lattice and mismatch. DFT calculations at 0 K give a hierarchy in the formation energies that promotes a competition between OR2 and OR1, the most stable having the lowest mismatch.

V. CONCLUSIONS

The epitaxial relationships between a gold deposit and Si(111) substrates were investigated using GIXS. At RT, a few-ML-thick deposit is found to result in a polycrystalline flat thin film. During the deposition, the out-of-plane epitaxies were found to be coverage dependent but with a large majority of the grains presenting the aligned epitaxy: Au(111) \parallel Si(111). For deposits larger than 2 ML, this out-of-plane epitaxial relationship was studied in more details and revealed three different in-plane orientation relationships: the parallel epitaxial relationship (OR1) and two others, OR2 and OR3, turned by 19.1° and 10.9° , respectively. The selection of the system among these three different configurations is temperature dependent. At RT, the OR1 is more favorable than the OR2 and the OR3 is not observed. At higher temperature (around 620 K), the OR2 is energetically favored compared to the OR1 and the OR3 appears. The dewetting process that transforms the thin film into gold islands thus takes place with a readjustment of the epitaxial configurations. This change in the ORs is due to differing thermal coefficients between the gold and the silicon substrate that modify the matching quality of the corresponding coincidence lattices. The experimental measurements are confirmed by *ab initio* calculations, revealing that the stability of the OR2 configuration is the most favorable.

Although the behavior of large deposits ($> 2 \text{ ML}$) seems rather clear, the peculiar case of small deposits ($\leq 2 \text{ ML}$) is less obvious and should be prone to further studies. Our current observations tend to reveal a size dependence of the ORs selection as the OR1 was found to be the preferred configuration at 620 K for islands formed by

dewetting of a 2-ML deposit. This could be explained by looking at the variation of the mismatch value along a single crystallographic row, which increases proportionally with the distance from the origin in perfect coincidence. Islands with small diameter would therefore not have to change their in-plane OR to compensate for the thermal expansion as the mismatch would be constrained to low values. No particular link was found between the epitaxial relationships found here in the solid state and the peculiar (6×6) reconstruction that

forms after annealing well above the eutectic temperature, inducing an enhanced supercooling of the AuSi eutectic droplets.

ACKNOWLEDGMENT

We deeply acknowledge the ESRF for providing beamtime and the BM32 beamline staff, especially O. Geaymond and O. Ulrich for their help in setting up the beamline and experiment.

*Corresponding author: gilles.renaud@cea.fr

- ¹G. Le Lay, *Surf. Sci.* **132**, 169 (1983).
- ²J. A. Venables, *Surf. Sci.* **299–300**, 798 (1994).
- ³R. S. Wagner and W. C. Ellis, *Appl. Phys. Lett.* **4**, 89 (1964).
- ⁴W. H. Chen, R. Lardé, E. Cadel, T. Xu, B. Grandidier, J. P. Nys, D. Stiévenard, and P. Pareige, *J. Appl. Phys.* **107**, 084902 (2010).
- ⁵D. Kim, A. L. Giermann, and C. V. Thompson, *Appl. Phys. Lett.* **95**, 251903 (2009).
- ⁶T. U. Schüllli, R. Daudin, G. Renaud, A. Vaysset, O. Geaymond, and A. Pasturel, *Nature (London)* **464**, 1174 (2010).
- ⁷O. G. Shpyrko, R. Streitl, V. S. K. Balagurusamy, A. Y. Grigoriev, M. Deutsch, B. M. Ocko, M. Meron, B. H. Lin, and P. S. Pershan, *Science* **313**, 77 (2006).
- ⁸O. G. Shpyrko, R. Streitl, V. S. K. Balagurusamy, A. Y. Grigoriev, M. Deutsch, B. M. Ocko, M. Meron, B. H. Lin, and P. S. Pershan, *Phys. Rev. B* **76**, 245436 (2007).
- ⁹A. L. Pinardi, S. J. Leake, R. Felici, and I. K. Robinson, *Phys. Rev. B* **79**, 045416 (2009).
- ¹⁰J. J. Lander, *Surf. Sci.* **1**, 125 (1964).
- ¹¹D. Dornisch, W. Moritz, H. Schulz, R. Feidenhansl, M. Nielsen, F. Grey, and R. L. Johnson, *Phys. Rev. B* **44**, 11221 (1991).
- ¹²R. Plass and L. D. Marks, *Surf. Sci.* **380**, 497 (1997).
- ¹³E. Bauer and H. Poppa, *Thin Solid Films* **12**, 167 (1972).
- ¹⁴F. Ruffino and M. G. Grimaldi, *J. Appl. Phys.* **107**, 104321 (2010).
- ¹⁵W. Swiech, E. Bauer, and M. Mundscha, *Surf. Sci.* **253**, 283 (1991).
- ¹⁶E. Jiran and C. Thompson, *Thin Solid Films* **208**, 23 (1992).
- ¹⁷B. Ressel, K. C. Prince, S. Heun, and Y. Homma, *J. Appl. Phys.* **93**, 3886 (2003).
- ¹⁸A. Kirakosian, J. L. Lin, D. Y. Petrovykh, J. N. Crain, and F. J. Himpsel, *J. Appl. Phys.* **90**, 3286 (2001).
- ¹⁹A. Rota, A. Martinezgil, G. Agnus, E. Moyen, T. Maroutian, B. Bartenlian, R. Megy, M. Hanbucken, and P. Beauvillain, *Surf. Sci.* **600**, 1207 (2006).
- ²⁰N. Ferralis, F. E. Gabaly, A. K. Schmid, R. Maboudian, and C. Carraro, *Phys. Rev. Lett.* **103**, 256102 (2009).
- ²¹N. Ferralis, R. Maboudian, and C. Carraro, *J. Am. Chem. Soc.* **130**, 2681 (2008).
- ²²E. Piscopiello, L. Tapfer, M. V. Antisari, P. Paiano, P. Prete, and N. Lovergine, *Phys. Rev. B* **78**, 035305 (2008).
- ²³J. B. Hannon, S. Kodambaka, F. M. Ross, and R. M. Tromp, *Nature (London)* **440**, 69 (2006).
- ²⁴S. Vasisht and J. Shirokoff, *Appl. Surf. Sci.* **256**, 4915 (2010).
- ²⁵S. Warren, P. Prod'homme, F. Maroun, P. Allongue, R. Cortes, C. Ferrero, T. Lee, B. Cowie, C. Walker, S. Ferrer, and J. Zegenhagen, *Surf. Sci.* **603**, 1212 (2009).
- ²⁶C. R. Chen and L. J. Chen, *Appl. Surf. Sci.* **92**, 507 (1996).
- ²⁷H. Dosch, *Critical Phenomena at Surfaces and Interfaces: Evanescent X-Ray and Neutron Scattering* (Springer, Berlin, 1992).
- ²⁸P. Mark, J. D. Levine, and S. H. McFarlane, *Phys. Rev. Lett.* **38**, 1408 (1977).
- ²⁹G. Kresse and J. Furthmuller, *Comput. Mater. Sci.* **6**, 15 (1996).
- ³⁰G. Kresse and D. Joubert, *Phys. Rev. B* **59**, 1758 (1999).
- ³¹F. C. Nix and D. MacNair, *Phys. Rev.* **60**, 597 (1941).
- ³²R. Daudin, C. Revenant, G. Davi, and G. Renaud, *Phys. E (Amsterdam)* **44**, 1905 (2012).
- ³³H. Hibino and Y. Watanabe, *Surf. Sci.* **588**, L233 (2005).
- ³⁴K. Fuchigami and A. Ichimiya, *Surf. Sci.* **357–358**, 937 (1996).
- ³⁵M. Jalochowski and E. Bauer, *Phys. Rev. B* **37**, 8622 (1988).
- ³⁶D. Katzel and K. Meinel, *J. Cryst. Growth* **98**, 690 (1989).
- ³⁷K. S. Kim, Y. W. Kim, N. G. Park, W. S. Cho, D. S. Choi, S. S. Kim, and C. N. Whang, *Nucl. Instrum. Methods Phys. Res., Sect. B* **117**, 289 (1996).
- ³⁸W. Lojkowski and H. J. Fecht, *Prog. Mater. Sci.* **45**, 339 (2000).
- ³⁹L. Vitos, A. V. Ruban, H. L. Skriver, and J. Kollar, *Surf. Sci.* **411**, 186 (1998).
- ⁴⁰C. Boragno, F. Buatier de Mongeot, R. Felici, and I. K. Robinson, *Phys. Rev. B* **79**, 155443 (2009).
- ⁴¹J. J. Yeh, J. Hwang, K. Bertness, D. J. Friedman, R. Cao, and I. Lindau, *Phys. Rev. Lett.* **70**, 3768 (1993).
- ⁴²Y. Hoshino, Y. Kitsudo, M. Iwami, and Y. Kido, *Surf. Sci.* **602**, 2089 (2008).
- ⁴³W. Bollmann and H.-U. Nissen, *Acta Crystallogr. Sect. A* **24**, 546 (1968).
- ⁴⁴U. Dahmen, *Acta Metall.* **30**, 63 (1982).
- ⁴⁵Y. Ikumura and P. Pirouz, *Mater. Sci. Forum* **207–209**, 121 (1996).